Journal Pre-proof

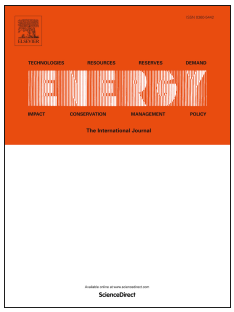

Entropy generation analysis based on a three-dimensional agglomerate model of an anion exchange membrane fuel cell

Bruno S. Machado, Mohamed Mamlouk, Nilanjan Chakraborty

PII: S0360-5442(19)32362-X

DOI: https://doi.org/10.1016/j.energy.2019.116667

Reference: EGY 116667

To appear in: *Energy*

Received Date: 28 May 2019

Revised Date: 30 September 2019

Accepted Date: 30 November 2019

Please cite this article as: Machado BS, Mamlouk M, Chakraborty N, Entropy generation analysis based on a three-dimensional agglomerate model of an anion exchange membrane fuel cell, *Energy* (2020), doi: https://doi.org/10.1016/j.energy.2019.116667.

Entropy generation analysis based on a three-dimensional agglomerate model of an anion exchange membrane fuel cell

Bruno S. Machado [1,*], Mohamed Mamlouk[1], Nilanjan Chakraborty [1]

[1]School of Engineering, Newcastle University, Newcastle-upon-Tyne, NE1 7RU, UK

Email: b.de-souza-machado1@newcastle.ac.uk (BSM)*; mohamed.mamlouk@newcastle.ac.uk (MM); nilanjan.chakraborty@newcastle.ac.uk (NC)

*Corresponding author. Tel: +44 191 208 6170

NOMENCLATURE

$a_{Pt/C}$	specific area, m^{-1}
A	active reaction area, m^2
ACL	anode catalyst layer
BP	bipolar plate
C	molar concentration, kmol m^{-3}
CL	catalyst layer
CCL	cathode catalyst layer
C_P	specific heat, J kg^{-1} K^{-1}
D_{ij}	Maxwell-Stefan diffusion coefficient matrix, m^2s^{-1}
D	mass diffusivity, m^2 s^{-1}
E_r	effectiveness factor
E_g	total energy in the gaseous phase, J kg^{-1}
EW	equivalent molecular weight of dry membrane, kg $kmol^{-1}$
F	Faraday's constant, C $kmol^{-1}$
GDL	gas diffusion layer
L_h	latent heat, J kg^{-1}
h	sensible enthalpy, J kg^{-1}
H	Henry´s constant, Pa m^2 mol^{-1}, largest dimension in the direction in question, m
i	volumetric current density, A m^{-3}
j_0	exchange current density, A m^{-2}
k	reaction rate coefficient, s^{-1}, thermal conductivity, W m^{-1} K^{-1}
k_p	permeability, m^2
L	volume fraction
m	mass loading, kg m^{-2}
$\dot{m}$	mass flow rate, kg s^{-1}
M	molecular weight, kg $kmol^{-1}$
M	membrane
n	number of electrons simultaneously release or uptake
n_d	electro osmotic drag coefficient
$\boldsymbol{N}$	diffusion flux of species, m^2 s^{-1}
n_d	electro osmotic drag coefficient
p	pressure, Pa
r	radius, m
R	universal gas constant, J $kmol^{-1}$ K^{-1}
RH	relative humidity
s	liquid water fraction
S	source terms, entropy J mol^{-1} K^{-1}
$\dot{S}$	rate of entropy, W K^{-1}
T	temperature, K
T_0	inlet temperature, K
$\boldsymbol{u}$	superficial velocity vector, m s^{-1}
V	voltage, V
X	mole fraction
Y	mass fraction

Greek letters

α	transfer coefficient
δ	thickness, m
γ	water phase change rate, s^{-1}
ϵ	porosity
ζ	water transfer rate, s^{-1}
η	overpotential, V
θ	contact angle, °
κ	electrical conductivity, S m^{-1}
λ	membrane water content
$\emptyset$	Thiele's modulus, non-dimensional minimum cell distance
μ	dynamic viscosity, kg m^{-1} s^{-1}
ξ	stoichiometry ratio

ρ	density, kg m^{-3}
ϕ	potential
Ψ	mode of entropy generation rate
Δ	cell size in the direction in question, m
$\bar{\bar{\tau}}$	viscous stress tensor, Pa

Subscript and Superscript

a	anode
agg	agglomerate
c	cathode, capillary
C	carbon
cond	condensation
d	dissolved
eff	effective
e	equilibrium
evap	evaporation
FC	fuel cell
g	gas phase
H_2	hydrogen
H_2O	water
IRV	irreversible heat
i	species
l	liquid phase
LH	latent heat
mass	mass
mem	membrane
m	membrane phase
M	ionomer
MT	mass transfer
out	output
OL	Ohmic loss
O_2	oxygen
Pt	platinum
ref	reference
REV	reversible heat
rev	reversible
sat	saturation
s	solid phase
spe	specific
TC	thermal conductivity
tot	total
VD	viscous dissipation
vl	vapour to liquid (vice-versa)

ABSTRACT

A three-dimensional agglomerate numerical model has been used to analyse entropy generation in an anion exchange membrane fuel cell. The effects of inlet relative humidity, platinum loading, carbon loading and ionomer volume fraction on entropy generation have been analysed in the present study. The reversible and irreversible heat have been identified as the main sources of entropy production for all the parameters tested. Even though the production of entropy due to Ohmic loss occurs due to both electronic and ionic potentials, the production of entropy as a result of the first is insignificant in comparison to the latter due to the fact that the electronic conductivity is significantly higher in comparison to the ionic diffusivity coefficient. A strong effect of the back diffusion of water has been found on the entropy production due to Ohmic loss, as the hydration of the membrane directly affects the anion transport through the membrane. Water condensation at the anode catalyst layer and gas diffusion layer has been observed in a few cases, giving rise to the entropy generation due to latent heat. Nevertheless, this has been observed to be 1 to 2 orders of magnitude lower in comparison to the entropy generated due to reversible, irreversible and Ohmic heats.

Keywords: Anion exchange membrane fuel cell; entropy generation; relative humidity; platinum loading; carbon loading; ionomer volume fraction.

1. INTRODUCTION

The anion exchange membrane (AEM) fuel cells offer a highly efficient economically feasible option for power generation without the emission of greenhouse gas. Significant advancements have been made in the experimental and numerical investigations of AEM in the last decade. Gupta et al. [1] has recently synthesized a soluble ionomer with an ion exchange capacity of 1.91 mmol g^{-1} and, at 100% relative humidity, an OH^- ionic conductivity of 0.14 and 0.18 S cm^{-1} has been achieved at 50 and 70^oC, respectively. In addition, several numerical models of AEM have been proposed in order to accurately reproduce experimental findings. Jiao et al. [2] developed a three-dimensional macro-homogenous model in order to provide physical insights into the water transportation within the fuel cell layers. Relative humidity at the inlet and operating temperature have been found to have significant impacts on the overall performance of the fuel cell, as the membrane hydration and the electrochemical kinetics are improved with the increases of both quantities [2]. The present authors proposed a macro-homogenous model in order to analyse the effects of flow direction, relative humidity and temperature on the overall performance of the fuel cell [3]. It has been found that the flow direction in the channel has no significant impact on the overall fuel cell performance [3]. Nevertheless, the macro-homogenous model does not account for the influences of the catalyst layer (CL) composition on the reaction rate. In addition to that, the transport mechanisms of species and ions within different parts in the CL have been severely simplified in the macro-homogenous model. Thus, a three-dimensional agglomerate model was proposed in [4] where its predictions have been compared to a macro-homogenous model, which revealed that the macro-homogenous model overpredicts the fuel cell overall performance in comparison to the agglomerate model. This difference originates from the concentration loss arising from the species diffusion through the ionomer layer and the correction of the ionic transportation by the volume fraction of platinum dispersed carbon. Moreover, the effectiveness factor for the anode catalyst layer (ACL) reveals a high utilisation of the ACL, whereas the cathode catalyst layer (CCL) exhibits a smaller effectiveness factor than anode due to slower diffusion of the oxygen on cathode side when compared to hydrogen diffusion on anode side. Later, a parametric analysis has been performed to analyse the influences of the CL composition (e.g. ionomer volume fraction, platinum and carbon loading) and relative

humidity on the overall fuel cell performance [5]. It has been found that, for the range of platinum loading considered (0.004 to 0.01 kg m^{-2}), an increase in the platinum loading enhances the overall performance of the fuel cell as the effective surface area per unit volume of the CL increases, and thus reduces the activation loss. An increase in carbon loading results in a thicker CL and consequently, an increase of the Ohmic loss has been observed. Moreover, a significant influence of the ionomer volume fraction on the overall performance of the AEM fuel cell has been observed, which reveals an augmentation of the overall performance when the ionomer volume fraction increases from 0.22 to 0.30, as the ionic diffusion within CLs is enhanced with increasing ionomer volume fraction.

Nevertheless, limited attention has been directed to the analysis of the irreversibility in the energy-conversion in fuel cells. Sciacovelli et al. [6] proposed an optimization of the overall performance of a solid oxide fuel cell through the analysis of the entropy generation. They identified the coupling between mass and heat transfer as the main contributor for the entropy generation, which dominates over the Ohmic entropy generation in SOFC operating at 973 K. At low temperature (e.g., <100°C) however, it is reported that the main source of irreversibility is the concentration loss, mainly due to the large variation of species throughout the domain. Range-Hernandez et al. [7] analysed the entropy generation in a proton exchange membrane (PEM) fuel cell. As excepted, the entropy generation has been observed to reach higher values at higher current density production where energy losses in the fuel cell increases and efficiency decrease. Naterer et al. [8] modelled numerically the entropy production due to Ohmic heat and concentration polarisation for SOFC and PEM fuel cell. They reported an increase in entropy production in PEM fuel cells when the current density is increased. Naterer et al. [8] related the rise in entropy production due to Ohmic loss and concentration polarisation to the increased flux of electrons and ions and the larger rates of reaction occurring at the catalyst layers, respectively. When analysing SOFCs, Naterer et al. [8] have observed a raise in entropy production when operating at low temperature (i.e. 650 K) as consequence of a decrease of the fuel cell performance. An one-dimensional model was used to analyse the local and total entropy production of a polymer electrolyte fuel cell [9], which revealed dependences of the entropy production and power output on the cathode catalyst layer overpotential [9]. Damian-Ascencio et al.

[10] proposed a PEM fuel cell with tree-like flow field channels and an entropy generation analysis has been performed. The authors concluded that the entropy generation due to mass diffusion dominates over entropy generation due to heat transfer and fluid friction (or viscous action). However, an entropy generation analysis is yet to be performed for a representative AEM fuel cell.

With the urge of clean technologies that supply electrical energy reliably, attention has been brought to fuel cells due to their advantages such as energy conversion potential, lack of greenhouse gas effect and modularity just to name a few. However, in order to address efficiently the current technical issues of AEM fuel cells, an entropy generation analysis is necessary to identify the main sources of entropy production (i.e. irreversibilities) so that it can enlighten future analyses on areas where there are potentials to significantly enhance the fuel cell performance. Hence, in this study, a three-dimensional agglomerate model for a representative AEM fuel cell has been used to perform an extensive analysis of the entropy generation due to reversible heat, irreversible heat, latent heat, mass diffusion, viscous dissipation, thermal conduction (alternatively can be said as thermal diffusion) and Ohmic resistance for different operating conditions.

2. NUMERICAL MODEL

In order to reduce computational efforts, a number of assumptions were made. Nevertheless, it is worth mentioning that the essential physics of a representative AEM fuel cell has not been compromised by these assumptions. The ideal gas law has been applied to the gaseous mixture and the membrane has been considered to be impenetrable to all species but water is considered to be a dissolved phase. The present model features an additional phase for liquid water, in the case of the partial pressure of water vapour has reached the saturation pressure and the condensation phenomenon took place. Finally, a steady state regime has been considered in this study and the flow is assumed to be laminar (i.e. Reynolds number in the order of 100). The bipolar plate (BP), flow channel (FC), gas diffusion layer (GDL), CL and membrane (M) components are presented in a schematic representation of the two-dimensional domain in Figure 1.

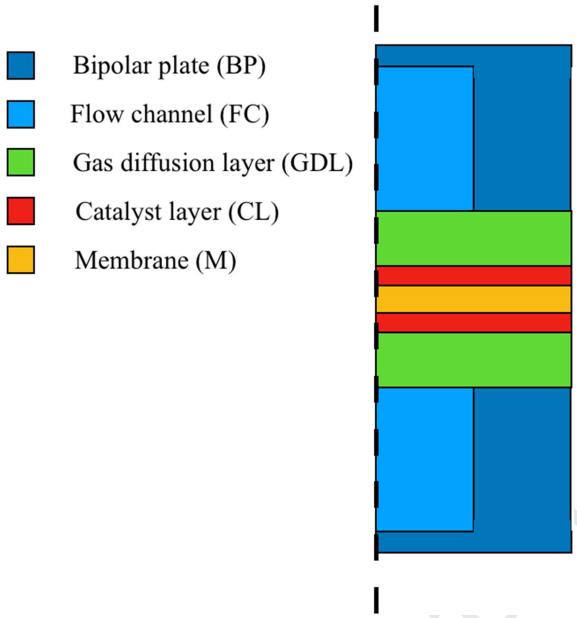

Figure 1 – Two-dimensional representation of a typical AEMFC.

The governing equations of this three-dimensional agglomerate model for an AEM fuel cell are given in Table 1 and the relevant equations and source terms are presented in this chapter. Interested readers are referred to Ref [5] for a detailed explanation of the governing equations, and the equations that are not provided here for the sake of conciseness.

Conservation Equation	Mathematical expression	Domain
Momentum	$\rho^g(\boldsymbol{u}^g \cdot \nabla \boldsymbol{u}^g) + \frac{\mu^g}{k_p}\boldsymbol{u}^g = -\nabla p + \nabla \cdot (\bar{\bar{\tau}})$	FC, GDL, CL
Species	$-\rho^g \boldsymbol{u}^g \cdot \nabla Y_i^g - \nabla \cdot \left[-\rho^g \sum_{j=1}^{N}(1-s) D_{ij}\left(\nabla X_j^g - Y_i^g\right)\frac{\nabla p}{p}\right] = S_i^g$	FC, GDL, CL
Mass	$-\nabla \cdot (\rho^g \boldsymbol{u}^g) = -\nabla \cdot \left(\rho^g \frac{k_p}{\mu^g}\nabla p\right) = S_{mass}$	FC, GDL, CL
Dissolved water	$-\nabla \cdot \left(\mathrm{D}_{\mathrm{d}}^{\mathrm{eff}} \nabla \lambda\right) + \nabla \cdot \left(\frac{EW}{\rho_{mem}}\frac{n_d}{F}\boldsymbol{J}_m\right) = S_{H_2O}^d$	CL, Membrane
Liquid water	$\nabla \cdot \left(-\frac{\rho^l s^3}{\mu^l}\frac{dp_c}{ds}\right)\nabla s + \nabla \cdot \frac{\rho^l \mu^g s^3}{\mu^l (1-s)^3}\boldsymbol{u}^g = S_{H_2O}^l$	GDL, CL
Solid phase potential	$-\nabla \cdot \left(\kappa_s^{eff} \nabla \phi_s\right) = S_s$	BP, GDL, CL

Ionic phase potential	$-\nabla \cdot \left(\kappa_m^{eff} \nabla \phi_m\right) = S_m$	CL, Membrane
Energy	$\nabla \cdot \left(\boldsymbol{u}^g(\rho^g E^g + p^g)\right) = \nabla \cdot \left(k^{eff} \nabla T - (\sum_i h_i \boldsymbol{N}_i) + (\bar{\bar{\boldsymbol{\tau}}} \cdot \boldsymbol{u}^g)\right) + S_E$	All domains

Table 1 – Governing equations and domains [4, 5].

In the agglomerate model, the volumetric current density at the anode and cathode CLs are described, respectively, as [11]

$$i_a = 2F\left(\frac{p_{H_2}}{H_{H_2}}\right)^{0.5}\left[\frac{1}{E_{r,a}k_a} + \frac{(r_{agg}+\delta_M)\delta_M}{a_{agg}r_{agg}D_{H_2-M}}\right]^{-1} \text{(for anode)} \quad (1)$$

$$i_c = 4F\frac{p_{O_2}}{H_{O_2}}\left[\frac{1}{E_{r,c}k_c} + \frac{(r_{agg}+\delta_M)\delta_M}{a_{agg}r_{agg}D_{O_2-M}}\right]^{-1} \text{(for cathode)} \quad (2)$$

where F is the Faraday constant; H_{H_2} and H_{O_2} stand for the Henry's constant for hydrogen and oxygen, respectively; the partial pressure of hydrogen and oxygen are represented by p_{H_2} and p_{O_2}, respectively; the diffusion coefficient through the ionomer for hydrogen and oxygen are given by D_{H_2-M} and D_{O_2-M}, respectively; $E_{r,a}$ and $E_{r,c}$ are the effectiveness factor for anode and cathode CL, respectively; δ_M is the thickness of the ionomer covering the agglomerate; r_{agg} and a_{agg} are the radius and the effective specific surface area of the agglomerate, respectively. The reaction rate coefficients for anode and cathode CL, k_a and k_c respectively, are defined as [12]

$$k_a = \left(\frac{a_{Pt,a}^{eff}}{2F}\right)\left[\frac{j_{0,a}^{ref}}{\left(C_{H_2}^{ref}\right)^{0.5}}\right]\left[\exp\left(\frac{n\alpha_a F}{RT}\eta\right) - \exp\left(\frac{n(1-\alpha_a)F}{RT}\eta\right)\right] \quad (3)$$

$$k_c = \left(\frac{a_{Pt,c}^{eff}}{4F}\right)\left[\frac{j_{0,c}^{ref}}{C_{O_2}^{ref}}\right]\left[\exp\left(\frac{n\alpha_c F}{RT}\eta\right) - \exp\left(\frac{n(1-\alpha_c)F}{RT}\eta\right)\right] \quad (4)$$

where the reference molar concentrations of hydrogen and oxygen are $C_{H_2}^{ref}$ and $C_{O_2}^{ref}$, respectively; $j_{0,a}^{ref}$ and $j_{0,c}^{ref}$ are the exchange current densities at the anode and cathode side, respectively; the anodic and cathodic charge transfer coefficients are α_a and α_c, respectively; n is the number of electrons simultaneously release or uptake; R is the universal gas constant; T is the temperature and η

is the overpotential. Finally, with the definition of the exchange current density, the source term of the governing equations can be specified. With respect of the species and mass conservation equations, the consumption and production of the gaseous species due to the electrochemical reaction are defined as follows:

$$S_{H_2} = -\frac{i_a}{2F} M_{H_2} \tag{5}$$

$$S_{O_2} = -\frac{i_c}{4F} M_{O_2} \tag{6}$$

$$S_{H_2O,c} = -\frac{i_c}{2F} M_{H_2O} \tag{7}$$

$$S_{H_2O,a} = \frac{i_a}{F} M_{H_2O} \tag{8}$$

With respect to the dissolved water, the source term for the governing equation takes into account the adsorption and desorption of water at the CLs and it is expressed as [13]

$$S^d_{H_2O} = \zeta_{mem}(\lambda_e - \lambda) \tag{9}$$

where ζ_{mem} is the water transfer rate; the membrane water content and the equilibrium membrane water content are λ and λ_e, respectively.

As previously mentioned in the assumptions, liquid water is formed when the partial pressure of water vapour reaches the saturation pressure. The aforementioned phenomenon is describes in source term of the liquid water conservation equation as [14]:

$$S_{vl} = \begin{cases} \gamma_{cond}\epsilon(1-s)\frac{M_{H_2O}}{RT}\left(p_{H_2O} - p_{sat}\right) & \text{if } p_{H_2O} \geq p_{sat} \\ \gamma_{evap}\epsilon s\frac{M_{H_2O}}{RT}\left(p_{H_2O} - p_{sat}\right) & \text{if } p_{H_2O} < p_{sat} \end{cases} \tag{10}$$

where the condensation and evaporation rate are γ_{cond} and γ_{evap}, respectively; ϵ is the porosity volume fraction; s is the volume fraction of liquid water within the pores; M_{H_2O} is the molecular weight of water species; p_{H_2O} and p_{sat} are the partial pressure of water vapour and saturation pressure, respectively.

The source terms of the electronic and ionic conservation equations describe the electrons and ions, respectively, consumed or formed at the CLs due to the electrochemical reaction and they are defined as:

$$S_s = \begin{cases} i_a & \text{if } ACL \\ -i_c & \text{if } CCL \end{cases} \quad (11)$$

$$S_m = \begin{cases} -i_a & \text{if } ACL \\ i_c & \text{if } CCL \end{cases} \quad (12)$$

2.1 Conservation of energy

The energy conservation equation is shown in Table 1. The first two terms on right-hand side represent energy transfer due to conduction ($k^{eff}\nabla^2 T$) and diffusive species transport ($\nabla \cdot \sum_i h_i \boldsymbol{N}_i$) respectively.

$$E^g = h - \frac{p^g}{\rho^g} + \frac{v^2}{2} \quad (13)$$

h_i is the sensible enthalpy of species i is defined as:

$$h_i = \int c_{p,i}\, dT \quad (14)$$

The third term represent the viscous work ($\nabla \bar{\bar{\boldsymbol{\tau}}} \cdot \boldsymbol{u}^g$). The source term, S_E, (W m^{-3}) is associated with four different sources of heat presented at the right side of Eq. (15): reversible heat (exothermic reaction of water formation), irreversible heat (anode/cathode reaction activation losses), Joule heat (ionic and electronic Ohmic losses) and latent heat (water sorption/desorption, vaporisation and condensation). The general form of the aforementioned source term is defined as:

$$S_E = q_{RE} + q_{IR} + q_{OL} + q_{LH} \quad (15)$$

The specific source terms for the energy conservation equation and they respective domain are presented in Table 2.

Source term	Domain	Eq.
$q_{REV} = i_a \frac{T\Delta S}{2F}$	ACL	(16)
$q_{IRV} = i\lvert\eta\rvert$	CL	(17)

$q_{OL} = \left(\|\nabla\phi_s\|^2\kappa_S^{eff} + \|\nabla\phi_m\|^2\kappa_m^{eff}\right)$	BP, GDL, CL, M	(18)
$q_{LH} = L_h\left(S_{vl} - \frac{\rho_{mem}}{EW}M_{H_2O}S_{vd}\right)$	GDL, CL	(19)

Table 2 – Specific source terms for the energy conservation equation and domains [4].

In the AEMFC system analysed in this study, the reversible heat of water formation reaction has been considered to be produced at the anode CL (161.2 J mol^{-1} K^{-1}) [2, 15]. Moreover, as one can see in Eqs. (1) and (2), the species partial pressure is taken into account when solving the reaction rate term and therefore it is inherently included in Eqs. (16) and (17).

2.2 Boundary condition

In this study, the representative AEM fuel cell has humidified hydrogen and oxygen supplied at anode and cathode inlet, respectively. The molar concentration of hydrogen and oxygen at the anode and cathode inlet are defined, respectively, as:

$$C_{H_2} = \frac{(p_a - RHp_{sat})}{RT_0} \quad (20)$$

$$C_{O_2} = \frac{0.21(p_c - RHp_{sat})}{RT_0} \quad (21)$$

where p is the inlet pressure. The inlet temperature, T_0, was kept constant (=333.15 K) in this study. From the hydrogen and oxygen molar concentrations, the mass flow rate at both anode and cathode inlet are computed, respectively, as:

$$\dot{m}_a = \frac{\rho_a^g \xi_a I_{ref} A}{2FC_{H_2}} \quad (22)$$

$$\dot{m}_c = \frac{\rho_c^g \xi_c I_{ref} A}{4FC_{O_2}} \quad (23)$$

where ξ_a (=1.1) and ξ_c (=2.0) are the stoichiometry ratios of the anode and cathode, respectively; I_{ref} (=1.5 A cm^{-2}) is the reference current density; ρ is the density of the gas mixture. Moreover, no-slip boundary condition has been specified at the walls in contact with the gaseous phase. With respect to

the boundary condition to the energy conservation equation, at the external surfaces of the anode and cathode bipolar plate a convective heat transfer boundary condition has been applied and the stream temperature and convective heat transfer are considered to be T_0 and 100 W m^{-2} K^{-1}, respectively [16]. The boundary condition for the electronic potential is specified at the external surfaces of the anode and cathode electrodes, and are presented, respectively, as [13]:

$$\phi_{s,a} = V_{rev} - V_{out} \tag{24}$$

$$\phi_{s,c} = 0.0 \tag{25}$$

where V_{rev} is the theoretical reversible voltage [5] and V_{out} is the output voltage. For the variables no specifically mentioned in this section, a zero-flux in the normal direction boundary condition has been specified.

2.3 Entropy generation

The entropy generation analysis was implemented as post-processing of simulation data reported in [5]. In this study, seven different modes of entropy generation rate ($\dot{S}_\alpha$) were considered: thermal conductivity, mass transfer, viscous dissipation, reversible heat, irreversible heat, Ohmic loss and latent heat. The total rate of entropy generation ($\dot{S}^{tot}$) is calculated as follows:

$$\dot{S}^{tot} = \sum_{\Psi=1}^{m} \int_{V_{FC}} \dot{S}_\Psi dV \tag{26}$$

where Ψ is index of the mode of entropy generation rate, m is the number of modes of entropy generation rate (for the current analysis it is 7 for $\Psi = \mathrm{REV, IRV, OL, LH, TC, MT, VD}$, which will be defined later in this paper); and V_{FC} is the total volume of the fuel cell. The specific rate of entropy generation ($\dot{S}^{spe}$) is calculated as follows:

$$\dot{S}^{spe} = \frac{\dot{S}^{tot}}{V_{FC}} \tag{27}$$

For a given mode of entropy generation rate, the specific rate of entropy generation is given by:

$$\dot{S}_{\Psi}^{spe} = \frac{\int_{V_\Psi} \dot{S}_\Psi^i dV_i}{V_\Psi} \tag{28}$$

where V_Ψ is the volume over which $\dot{S}_\Psi^i$ is applicable.

The local rate of entropy generation due to thermal conduction is defined as [10]:

$$\dot{S}_{HT} = \frac{k}{T^2}\left[\left(\frac{\partial T}{\partial x}\right)^2 + \left(\frac{\partial T}{\partial y}\right)^2 + \left(\frac{\partial T}{\partial z}\right)^2\right] \quad (29)$$

where k is the thermal conductivity (W m^{-1} K^{-1}) and T is the temperature (K).

The rate of entropy generation due to mass transfer is given by [17]:

$$\dot{S}_{MT} = \sum_{i=1}^{N} \rho_i^g D_i^g \frac{R}{X_i M_i}\left(\frac{\partial X_i}{\partial x}\frac{\partial Y_i}{\partial x} + \frac{\partial X_i}{\partial y}\frac{\partial Y_i}{\partial y} + \frac{\partial X_i}{\partial z}\frac{\partial Y_i}{\partial z}\right) \quad (30)$$

where ρ_i^g and D_i^g are the gas density and mass diffusion coefficient for the ith species, respectively; R is the universal gas constant (8315 J kmol^{-1} K^{-1}); M_i is the molecular weight of the ith species; X_i and Y_i are the mole fraction and mass fraction of the ith species, respectively.

The rate of entropy generation due to viscous dissipation is obtained deriving from the viscous tensor term in the momentum conservation equation and it is given by [6]:

$$\dot{S}_{VD} = \frac{\mu^g}{T}\left\{\left[2\left\{\left(\frac{\partial u}{\partial x}\right)^2 + \left(\frac{\partial v}{\partial y}\right)^2 + \left(\frac{\partial w}{\partial z}\right)^2\right\} + \left(\frac{\partial u}{\partial y} + \frac{\partial v}{\partial x}\right)^2 + \left(\frac{\partial u}{\partial z} + \frac{\partial w}{\partial x}\right)^2 + \left(\frac{\partial v}{\partial z} + \frac{\partial w}{\partial y}\right)^2\right] - \frac{2}{3}\left(\frac{\partial u}{\partial x} + \frac{\partial v}{\partial y} + \frac{\partial w}{\partial z}\right)^2\right\} \quad (31)$$

where μ^g is the dynamic viscosity.

From the source term (Eq. (15)) of the energy conservation equation presented in Table 1, one can see that heat is generated due to the reversible and irreversible losses. Therefore, reversible and irreversible heat are accounted in the rate of entropy generation, respectively, as:

$$\dot{S}_{REV} = \frac{q_{REV}}{T} = i_a \frac{\Delta S}{2F} \quad (32)$$

$$\dot{S}_{IRV} = \frac{q_{IRV}}{T} = \frac{i|\eta|}{T} \quad (33)$$

Due to the transportation of charged species (ions and electrons) in conductive regions of the fuel cell, a rate of entropy generation term due to the Ohmic loss is calculated from Eq. (16) as [6]:

$$\dot{S}_{OL} = \frac{q_{OL}}{T} = \frac{1}{T}\left[\left(\kappa_m^{eff}\nabla\phi_m\right)\cdot\nabla\phi_m + \left(\kappa_s^{eff}\nabla\phi_s\right)\cdot\nabla\phi_s\right] \quad (34)$$

where κ_m and κ_s are the ionic and electronic diffusivity, respectively; ϕ_m and ϕ_s are the ionic and electronic potential, respectively.

Finally, the rate of entropy generation due to the heat generated from the water sorption/desorption, vaporisation and condensation phenomena (latent heat) is defined as

$$\dot{S}_{LH} = \frac{q_{LH}}{T} = \frac{L_h}{T}\left(S_{vl} - \frac{\rho_{mem}}{EW} M_{H_2O} S_{vd}\right) \quad (35)$$

2.4 Numerical procedure

The numerical model used in this study has been implemented in the commercial software ANSYS Fluent by the use of user defined functions (UDFs). The SIMPLE algorithm was used to link velocity and pressure. Second order central difference and upwind schemes were used to the diffusive and convective terms, respectively. The convergence criterion has been specified as 5×10^{-7} and a 1.5% maximum uncertainty to the current density was observed. In the present study, a mesh containing 10, 15 and 100 volumes in x, y and z direction, respectively, has been used and its characterization is presented in Table 3.

	$\emptyset_x$	$\emptyset_y$	$\emptyset_z$	r_x	r_y	r_z
BP	0.1	2.643×10^{-5}	0.01	1	1.211	1
FC		2.643×10^{-5}			1.211	
GDL		5.286×10^{-6}			1.211	
CL		2.643×10^{-7}			1.211	
Membrane		7.400×10^{-7}			1.211	

Table 3 – Non-dimensional minimum cell distance (i.e. $\emptyset = \Delta_{min,cell}/H$ where H is the largest dimension in the direction in question) and grid expansion ratio (r) values for the mesh used in this study.

The validation of the numerical model used in the present study has been done by qualitative comparison with experimental studies on AEM fuel cell. Due to the lack of data and the limited

information regarding the components of an AEM fuel cell, a direct quantitative comparison would not be possible. However, as one can see in Figure 2, the numerical model used in this study has qualitatively followed the trend observed for experimental studies [18-20]. Detailed information regarding the validation of the model can be found in Refs. [4, 5].

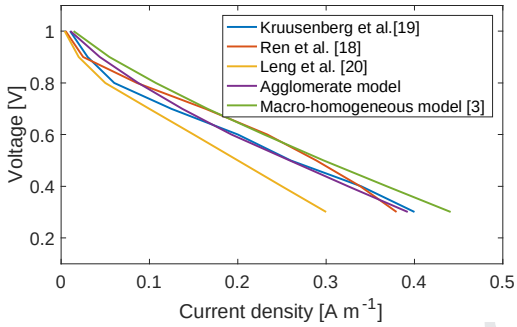

Figure 2 - Polarization curve for the agglomerate model and the experimental data [18-20].

3. RESULTS AND DISCUSSION

An analysis of the rate of entropy generation in a three-dimensional agglomerate model for an AEM fuel cell is performed in order to evaluate the irreversibility on the fuel cell overall performance. The effects of relativity humidity, platinum and carbon loading and ionomer volume fraction on the different entropy generation mechanisms have been analysed in this study. The complete set of parameters is presented in Table 4.

	RH_a (%)	RH_c (%)	m_{Pt} (kg m^{-2})	m_C (kg m^{-2})	L_M	δ_{CL} (m)
Case 1	95	50	0.004	0.006	0.22	1.00×10^{-5}
Case 2	50					
Case 3	50	95				
Case 4	70	70				
Case 5	95	50	0.006			
Case 6			0.01			
Case 7			0.004	0.016		2.39×10^{-5}
Case 8				0.0026		4.29×10^{-6}
Case 9				0.006	0.15	7.82×10^{-6}
Case 10					0.30	1.17×10^{-5}

Table 4 – Simulation cases. Case 1 is the base case. Grey cells represent the different values used in this parametric analysis [1, 11, 21-23].

The total rate of entropy generation $\dot{S}^{tot}$ and specific rate of entropy generation $\dot{S}^{spe}$ for 0.4, 0.6 and 0.8 V cell voltage are presented in Figure 3. As one can see in Figure 3, Case 2 shows a significant reduction of 13% (=2.03×10^{-3} W K^{-1}) in comparison to Case 1 (=2.39×10^{-3} W K^{-1}) when analysing the total rate of entropy generation. The most significant increase in the rate of entropy generation in comparison to the base case has been observed in Case 6, with a total of 19% increase (2.86×10^{-3} W K^{-1}). Similarly, when analysing the specific rate of entropy generation, one can observe a significant variation in comparison to the base case (Case 1). The specific rate of entropy generation varies significantly when comparing different cases. In comparison to Case 1 (=8395 W K^{-1} m^{-3}), for the 0.4 V cell voltage case, Case 2 shows a reduction of 16% on the specific rate of entropy generation produced (=7112 W K^{-1} m^{-3}). On the other hand, Case 6 shows an increase of 13% on the specific rate of entropy generated (=10037 W K^{-1} m^{-3}). Further details of the contribution of the different modes of entropy generation are presented in the following sections.

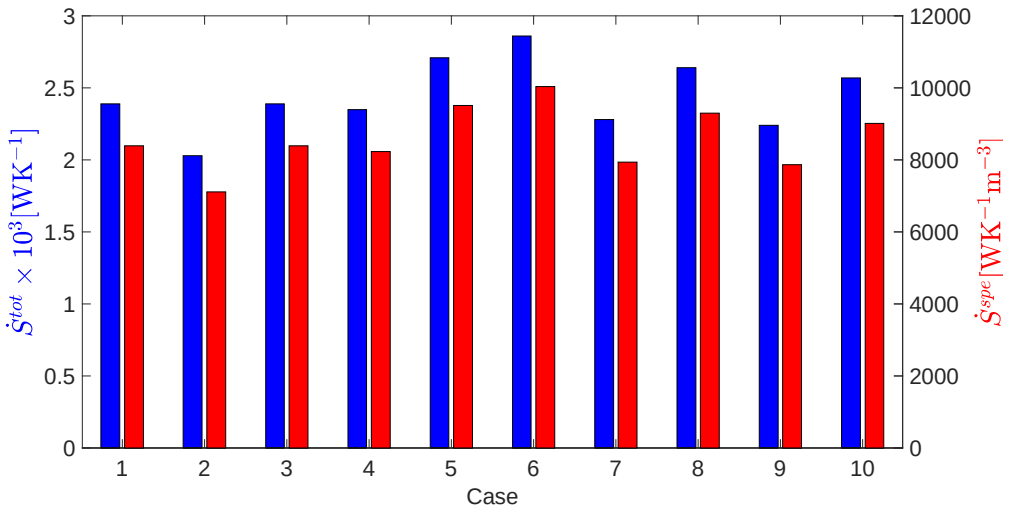

a)

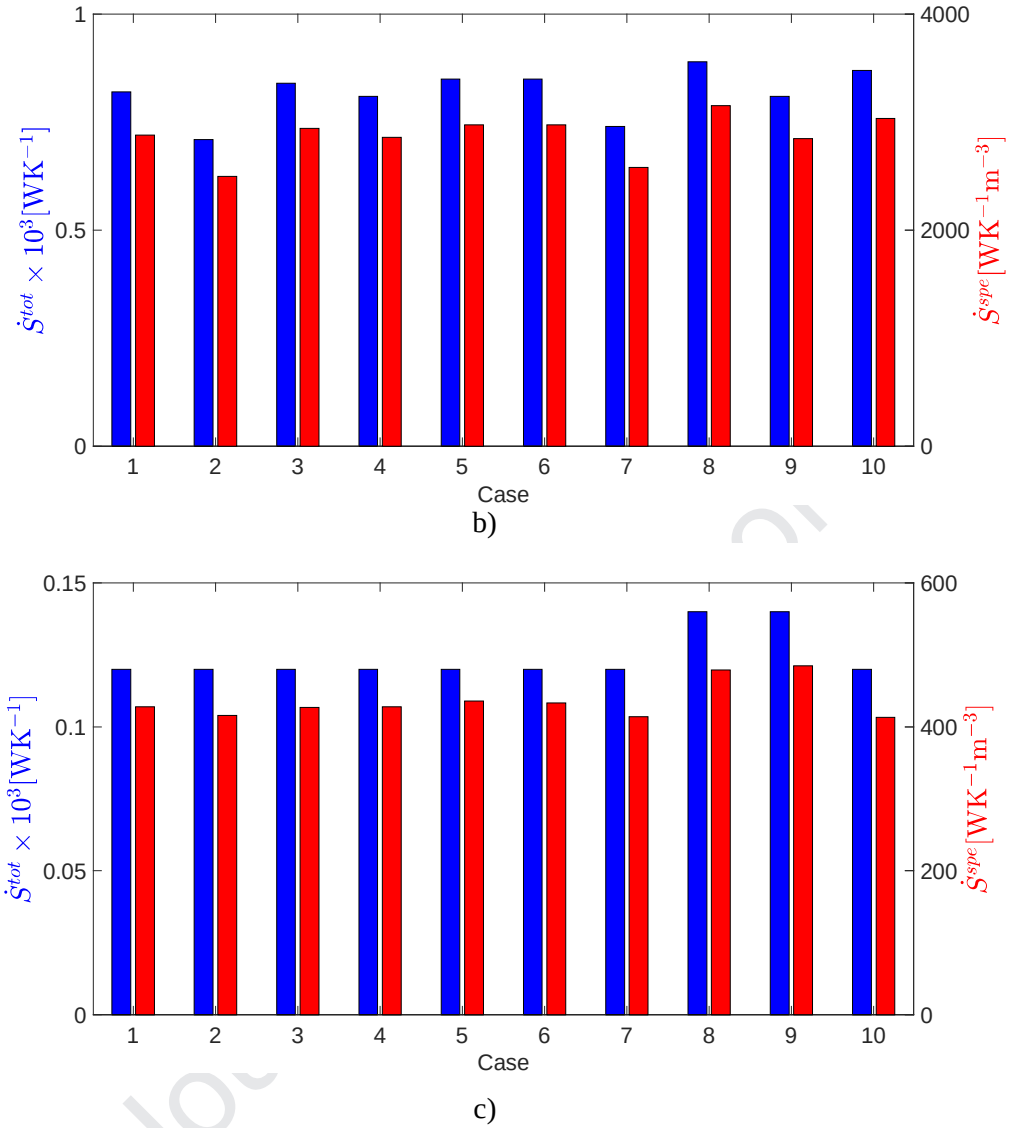

Figure 3 –Total rate of entropy generation (blue) and specific rate of entropy generation (red) for: a) 0.4 V b) 0.6 V and c) 0.8 V cell voltage.

3.1 Relativity humidity

Figure 4 presents the effects of the inlet relative humidity on the total entropy generation rate $\dot{S}^{tot}$ and specific rate of entropy generation for different modes (i.e. $\dot{S}_{\Psi}^{spe}$ for Ψ=REV,IRV,OL,LH,TC+MT+VD) for 0.4, 0.6 and 0.8 V cell voltages. Figure 4 shows that, for 0.4 V cell voltage, Case 1 (RH_a=95 %, RH_c=50 %) has the highest value of total rate of entropy generation among the cases studied: Cases 2 (RH_a=50 %, RH_c=50 %), Case 3 (RH_a=50 %, RH_c=95 %) and 4 (RH_a=70 %, RH_c=70 %), with entropy generation rates of 0.64×10^{-3}, 1.38×10^{-3} and

0.36×10^{-3} W K^{-1} due to reversible, irreversible and Ohmic heat, respectively. On the other hand, Case 2 showed the smallest total rate of entropy generation due to reversible, irreversible and Ohmic heat, mainly due to the lower relative humidity values at the anode and cathode inlets in comparison to Cases 1, 3 and 4. From Eq. (33), one can see that the entropy generation rate due to Ohmic loss is dependent on the electronic and ionic gradients. However, even though the transports of electrons and ions have been accounted for this term, the electronic contribution is insignificant (~2 to 3 orders of magnitude smaller) in comparison to the ionic contribution. Therefore, this term is mainly affected by the ionic transport in the CLs and membrane. As the ionic diffusion coefficient is directly related to the membrane hydration, it is necessary to have a good water management in order to maintain it hydrated and maintain favourable conditions for the purpose of ionic diffusion. The depletion of the membrane hydration in Case 2 at 0.4 V cell voltage due to weak back diffusion decreases the membrane ionic conductivity to 3.30 S m^{-1} in comparison to the 5.04 S m^{-1} from Case 1, causing a rise in the Ohmic loss from 0.23 V to 0.27 V, respectively. Moreover, the overpotential (η) in Eqs. (3) and (4) is driven by the ionic and electronic potentials. Thus, the rate of entropy generation due to reversible and irreversible heat is negatively affected, being reduced to 0.54×10^{-3} and 1.13×10^{-3} W K^{-1}, respectively. Case 3 has been observed to have slightly lower values of rate of entropy generation in comparison to Case 1. Due to the higher relative humidity supplied at the cathode inlet in comparison to the anode side, the membrane water content transport (i.e. diffusion and back diffusion) is negatively affected, and thus reducing the membrane ionic conductivity from 5.04 to 4.38 S m^{-1}, when comparing Case 3 and Case 1, respectively. This consequently reduces the total rate of entropy generation due to Ohmic heat to 0.36×10^{-3} W K^{-1}. Moreover, a rise of the total rate of entropy generation due to latent heat has been observed in Case 3 (0.02×10^{-3} W K^{-1}) in comparison to Case 1 (0.004×10^{-3} W K^{-1}). This is associated with the rise of the water partial pressure relative to the saturation pressure due to the combination of lower average back diffusion and the liquid water formation (i.e. average liquid water volume fraction of 0.10) as the product of the electrochemical reaction at the anode catalyst layer.

At 0.6 and 0.8 V cell voltages, one can see from Figure 4b and 4c, respectively, that, as expected. the contribution of the Ohmic loss to the total rate of entropy generation becomes less significant in comparison to the total rate of entropy generation due to reversible and irreversible heats. This behaviour originates due to the fact that most of the dominant energy losses at low overpotential/low currents is the kinetic rather than the ohmic losses. Moreover, one can observe that for the 0.6 V cell voltage, Case 2 exhibits the highest amount of entropy generation due to Ohmic loss. As shown in Figs. 5a and 5b, the ionic potential for Case 1 is more evenly distributed than in Case 2. Therefore, the rise in the gradient of ionic potential in Case 2 causes an augmentation of the entropy generation produced due to Ohmic loss. The aforementioned behaviour is also observed at 0.8V cell voltage, which is not shown here for the sake of brevity. Since the volume of the four cases compared in Fig. 4 is the same, no comparison of specific rate of entropy generation is presented in this section for the sake of brevity.

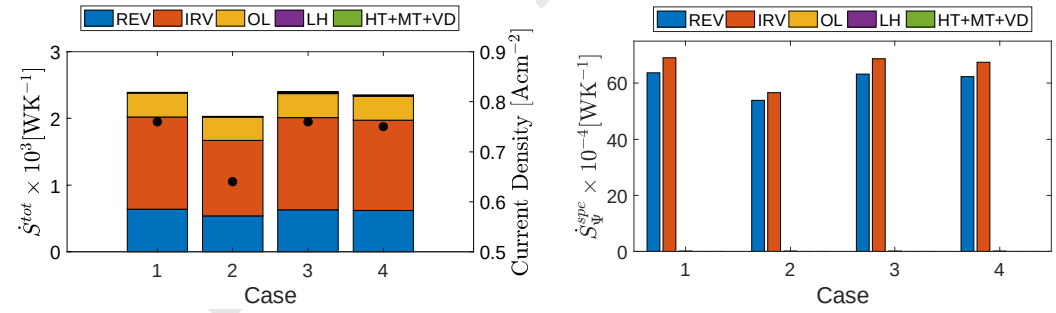

a)

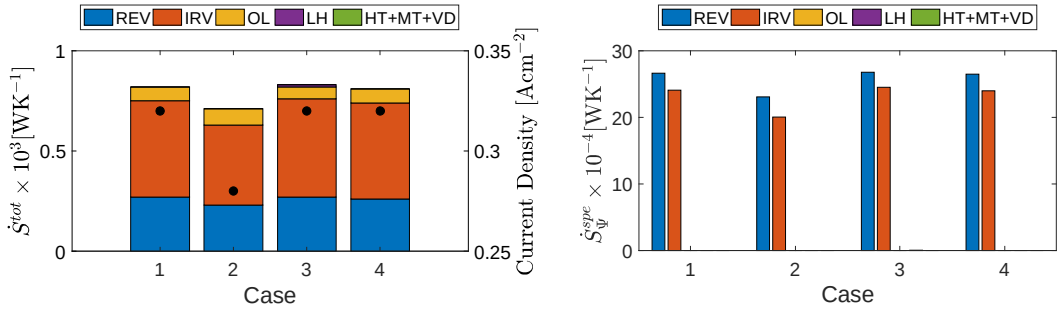

b)

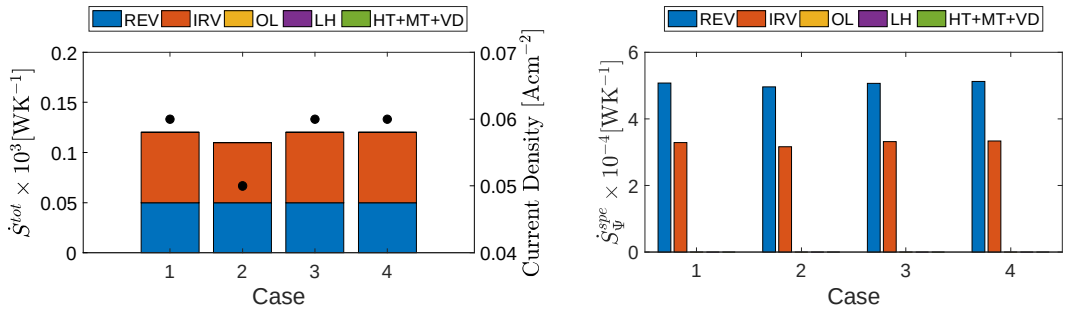

c)

Figure 4 – Total rate of entropy generation (shown by bars) and current density (shown by dots) (left) and specific rate of entropy generation (right) at different cell voltages: a) 0.4V, b) 0.6V and c) 0.8V for different inlet relative humidity: Case 1 ($RH_a = 95\,\%, RH_c = 50\,\%$), Case 2 ($RH_a = 50\,\%, RH_c = 50\,\%$), Case 3 ($RH_a = 50\,\%, RH_c = 95\,\%$) and Case 4 ($RH_a = 70\,\%, RH_c = 70\,\%$).

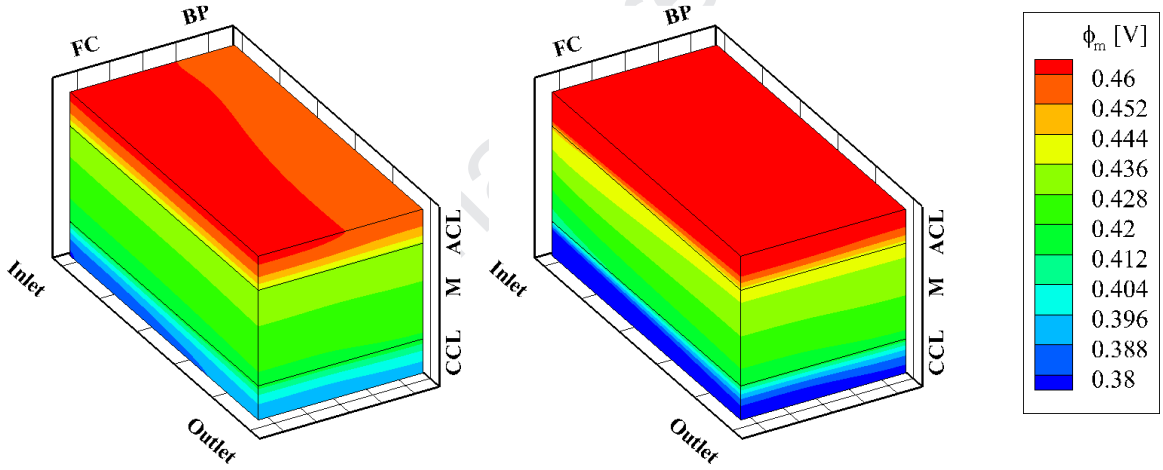

a) b)

Figure 5 – Ionic potential distribution for Case 1 and Case 2 at 0.6 V cell voltage.

3.2 Platinum loading

The effects of platinum loading on the total entropy generation rate $\dot{S}^{tot}$ and specific rate of entropy generation for different modes (i.e. $\dot{S}_{\Psi}^{spe}$ for Ψ=REV,IRV,OL,LH,TC+MT+VD) are presented in Fig. 6. The cases compared in this section exhibited no variation of the total volume of the fuel cell as the catalyst layer thickness remained almost constant with variation of Pt loading and will therefore be compared only in terms of the total rate of entropy generation $\dot{S}^{tot}$. As shown in Fig. 6a, Cases 5

(m_{pt}=0.006 kg m^{-2}) and 6 (m_{pt}=0.01 kg m^{-2}) showed an increase in the total rate of entropy generation in comparison to Case 1 (m_{pt}=0.004 kg m^{-2}). This is mainly associated to the increase of current density produced by Cases 5 (0.83 A cm^{-2}) and 6 (0.65 A cm^{-2}) in comparison to Case 1 (0.762 A cm^{-2}), caused by an increase of the effective surface area per unit of volume of the catalyst layer. Nevertheless, in terms of the percentage, the three main contributors to the total rate of entropy generation (i.e. reversible, irreversible and Ohmic heat) remained unaltered. Nevertheless, it can be discerned from Fig. 6b (0.6 V cell voltage) that an increase in total rate of entropy generation $\dot{S}^{tot}$ due to latent heat for Case 5 (0.011× 10^{-3} W K^{-1}) and 6 (0.012× 10^{-3} W K^{-1}) has been obtained. This behaviour is associated with the condensation of water within the anode catalyst layer and gas diffusion layer due to the increase of water formation as the product of the electrochemical reaction. As one can see from Fig. 6, since the total volume of the fuel cell for Case 1, 5 and 6 are the same, there is no difference in percentages between the different entropy generations mechanism when comparing the total and specific rates of entropy generations.

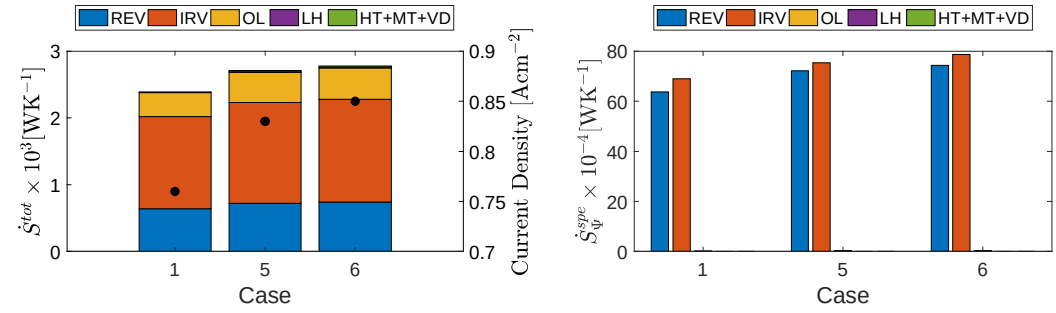

a)

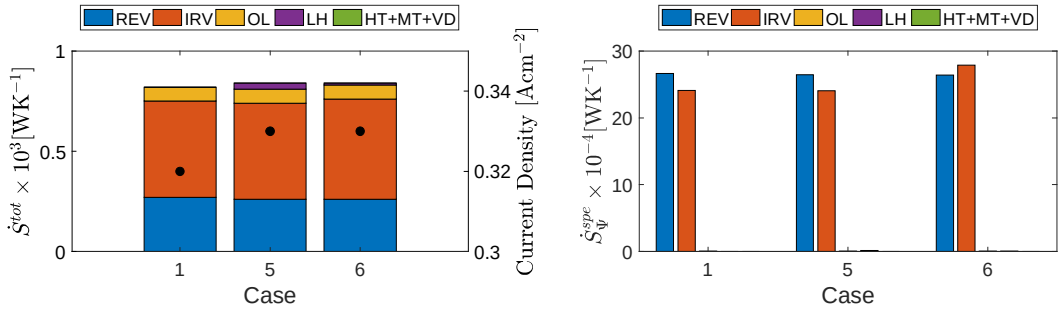

b)

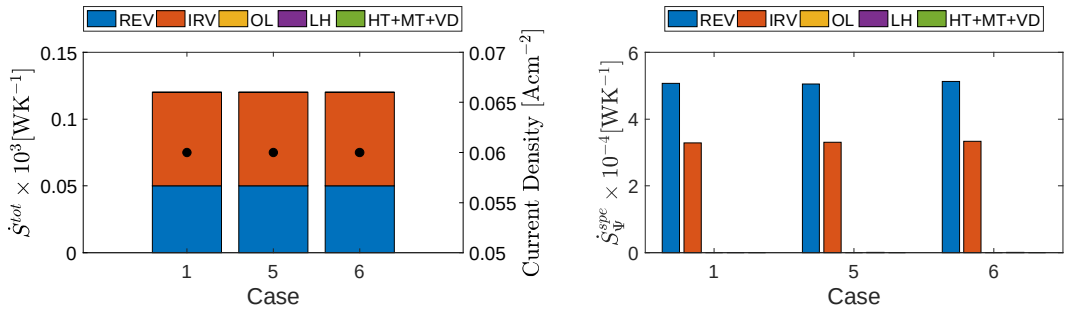

c)

Figure 6 – Total rate of entropy generation (shown by bars) and current density (shown by dots) (left) and specific rate of entropy generation (right) at different cell voltages: a) 0.4V, b) 0.6V and c) 0.8V for different platinum loadings: Case 1 (m_{pt}=0.004 kg m^{-2}), Case 5 (m_{pt}=0.006 kg m^{-2}) and Case 6 (m_{pt}=0.01 kg m^{-2}).

3.3 Carbon loading

The effects of carbon loading on the total entropy generation rate $\dot{S}^{tot}$ and specific rate of entropy generation for different modes (i.e. $\dot{S}_{\Psi}^{spe}$ for Ψ=REV,IRV,OL,LH,TC+MT+VD) are presented in Fig. 7. It is worth mentioning that the catalyst layer thickness varies depending on the carbon loading and therefore, the total volume of the AEM fuel cell changes accordingly [5]. As one can see in Fig. 7a, Case 7 (m_C=0.016 kg m^{-2} and δ_{CL}=2.39 × 10^{-5} m) exhibits a smaller extent of total entropy generation rate than in Case 1 (m_C=0.006 kg m^{-2} and δ_{CL}=1.00× 10^{-5} m) and Case 8 (m_C=0.0026 kg m^{-2} and δ_{CL}=4.29× 10^{-6} m). For the 0.4 cell voltage, the current density produced in Case 7 (0.663 A cm^{-2}) is smaller than in Case 1 (0.762 A cm^{-2}), and thus one can observe a reduction in the total rate of entropy generation due the reversible (=0.59× 10^{-3} W K^{-1}) and irreversible (=1.22× 10^{-3} W K^{-1}) heats, as shown in Fig. 7a. An opposite behaviour is observed in Case 8 (0.810 A cm^{-2}) and an increase in the total rate of entropy due to reversible (=0.68× 10^{-3} W K^{-1}) and irreversible (=1.49× 10^{-3} W K^{-1}) heats has been observed. The total rate of entropy generation due to Ohmic heat in Case 7 has been observed to be 0.40× 10^{-3} W K^{-1}, which, in comparison to the base case (Case 1) and Case 8 (0.38× 10^{-3} W K^{-1}), corresponds to an increase of 10 and 3%, respectively. The increase in

the total rate of entropy generation due to latent heat in Case 7 (0.06×10^{-3} W K^{-1}) and 8 (0.08×10^{-3} W K^{-1}) is caused by the condensation phenomenon at the anode catalyst layer and gas diffusion layer. For Case 8, the average liquid water volume fraction has been found to be 0.191, whereas it has been observed to be 0.100 in Case 1. From the previous analysis, for the 0.4 V cell voltage, one can observe a variation as high as 11% of the total rate of entropy generation in comparison to the base case (Case 1). Similar variation has also been observed when the specific rates of entropy generation for Cases 1, 7 and 8 are compared. However, when comparing the specific rate of entropy generation of different modes, reversible and irreversible heat modes have been found to increase significantly in comparison with other modes. Case 7 shows significant lower values for specific rate of entropy generation due to reversible (=246030 W K^{-1} m^{-3}) and irreversible (=256992 W K^{-1} m^{-3}) heat modes in comparison to Case 1 ($\dot{S}_{REV}^{spe}$=636723 W K^{-1} m^{-3} and $\dot{S}_{IRV}^{spe}$=690131 W K^{-1} m^{-3}). On the other hand, Case 8 exhibits the values of specific rate of entropy generation due to reversible ($\dot{S}_{REV}^{spe}$=1003063 W K^{-1} m^{-3}) and irreversible ($\dot{S}_{IRV}^{spe}$=1739965 W K^{-1} m^{-3}) heat modes, which are significantly greater than the base case. This large variation of the values in Cases 7 and 8 is mainly attributed to the variation of volume observed in the catalyst layer due to the different carbon loadings considered in this study. With respect to the specific rate of entropy generation due to Ohmic heat mode, the same trend has been observed in comparison to the total rate of entropy generation. However, the Ohmic heat is considerably less significant, being 2 to 3 orders of magnitude smaller in comparison to the specific sources of entropy due to reversible and irreversible heat modes. Moreover, the specific rate of entropy generated due to latent heat mode for Case 8 increases significantly ($\dot{S}_{LH}^{spe}$=3742 W K^{-1} m^{-3}) in comparison to Case 1 ($\dot{S}_{LH}^{spe}$=193 W K^{-1} m^{-3}), overcoming the contribution of the Ohmic heat mode ($\dot{S}_{OH}^{spe}$=2080 W K^{-1} m^{-3}) of the specific rate of entropy generation.

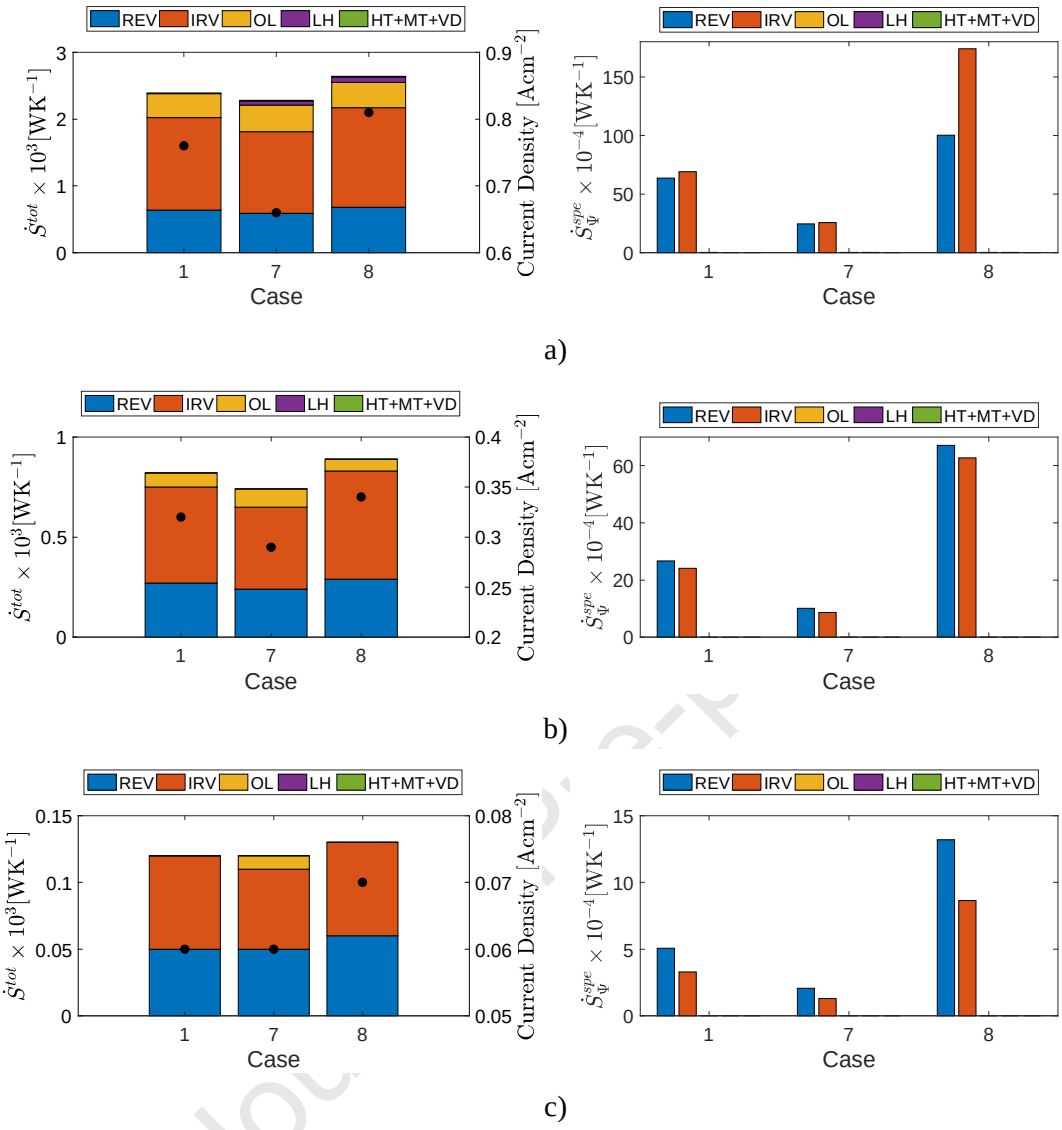

Figure 7 - Total rate of entropy generation (shown by bars) and current density (shown by dots) (left) and specific rate of entropy generation (right) at different cell voltages: a) 0.4V, b) 0.6V and c) 0.8V for different carbon loadings: Case 1 (m_C=0.006 kg m^{-2} and δ_{CL}=1.00× 10^{-5} m), Case 7 (m_C=0.016 kg m^{-2} and δ_{CL}=2.39× 10^{-5} m) and Case 8 (m_C=0.0026 kg m^{-2} and δ_{CL}=4.29× 10^{-6} m).

3.4 Ionomer volume fraction

Figure 8 shows the effects of ionomer loading on the total entropy generation rate $\dot{S}^{tot}$ and specific rate of entropy generation for different modes (i.e. $\dot{S}_{\Psi}^{spe}$ for Ψ=REV,IRV,OL,LH,TC+MT+VD). Since the current density produced in Case 9 (L_m=0.15 and δ_{CL}=7.82× 10^{-6} m) is smaller than in Case 1

(L_m=0.22 and δ_{CL}=1.00× 10^{-5} m) from 0.762 to 0.701 A cm^{-2}, a decrease of the total rate of entropy generation has been observed. As expected, both total rate of entropy generation due to reversible (=0.59× 10^{-3} W K^{-1}) and irreversible (=1.25× 10^{-3} W K^{-1}) heats in Case 9 decrease in comparison to Case 1. Even though the catalyst layer thickness has been reduced in comparison to the base case (Case 1), the total rate of entropy generation due to Ohmic heat (=0.38× 10^{-3} W K^{-1}) increases when compared to Case 1 (0.36× 10^{-3} W K^{-1}). This is attributed to the augmentation of the resistance to the ionic transport due to the reduction of the ionomer loading. Case 10 (L_m=0.30 and δ_{CL}=1.17× 10^{-5} m) exhibits an increase in total rate of entropy generation due to reversible (=0.68× 10^{-3} W K^{-1}), and irreversible (=1.47× 10^{-3} W K^{-1}) heats. Moreover, despite the enhancement of the ionic diffusion in the catalyst layer due to the increase of the ionomer loading, the total rate of entropy generation due to Ohmic heat increases to 0.41× 10^{-3} W K^{-1}, mainly due to the increase of the catalyst layer thickness. In terms of specific rate of entropy generation for different modes, even though Case 9 exhibits a drop in current density in comparison to other cases, the thinner catalyst layer contributed to the augmentation of the specific rate of entropy generation due to reversible ($\dot{S}_{REV}^{spe}$=749815 W K^{-1} m^{-3}) and irreversible ($\dot{S}_{IRV}^{spe}$=801329 W K^{-1} m^{-3}) heats. An opposite behaviour has been observed in Case 10, where high values of specific rate of entropy production due to reversible ($\dot{S}_{REV}^{spe}$=579469 W K^{-1} m^{-3}) and irreversible ($\dot{S}_{IRV}^{spe}$=626560 W K^{-1} m^{-3}) heat modes arise mainly due to the thicker catalyst layer. The specific rate of entropy production due to Ohmic heat mode has been observed to be as low as 0.1 and 0.2% for Case 9 and Case 10, respectively.

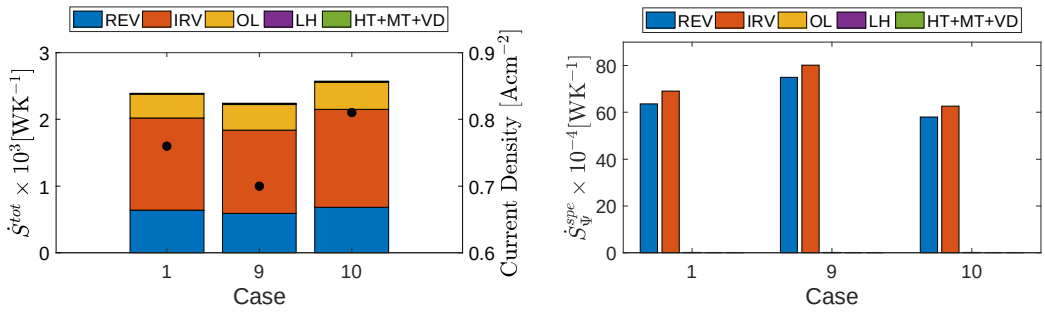

a)

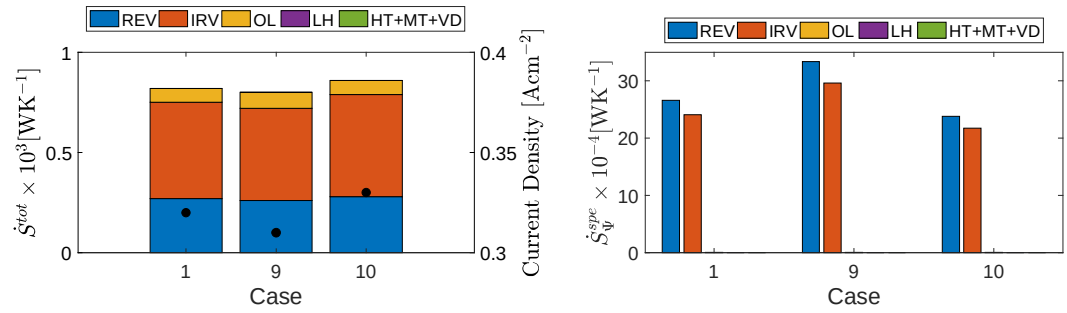

b)

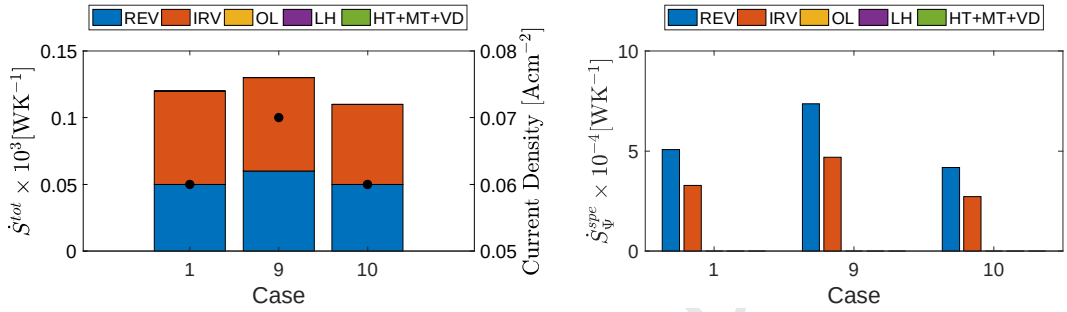

c)

Figure 8 – Total rate of entropy generation (shown by bars) and current density (shown by dots) (left) and specific rate of entropy generation (right) at different cell voltages: a) 0.4V, b) 0.6V and c) 0.8V for different ionomer loadings: for Case 1 (L_m=0.22 and δ_{CL}=1.00× 10^{-5} m), Case 9 (L_m=0.15 and δ_{CL}=7.82× 10^{-6} m) and Case 10 (L_m=0.30 and δ_{CL}=1.17× 10^{-5} m).

4. CONCLUSIONS

A three-dimensional agglomerate numerical model has been utilised to perform a numerical investigation of the different mechanisms of entropy generation with respect of the inlet relative humidity, platinum and carbon loading and ionomer volume fraction in an anion exchange fuel cell. For the 0.4 V cell voltage, the inlet relative humidity has been observed to significantly influence the total rate of entropy generation. The ionic transport produces greater amount of entropy in comparison to the electronic potential, as the ionic diffusion coefficient is significantly smaller in comparison to the electronic diffusion coefficient. Moreover, the relative humidity at the inlet has strong influences on the back diffusion and, consequently, the ionic diffusion coefficient is affected.

Increasing the platinum loading causes the reduction of the pores at the CL and the higher current density for high platinum loading results in the condensation of water vapour at the anode CL and GDL. This leads to an increase in the entropy generation due to latent heat. The higher current density also increases the total entropy generation due to the Ohmic loss as an augmentation of ions transportation through the membrane is observed.

The increase of the carbon loading (Case 7) leads to a decrease in total rate of entropy generation in comparison to Case 1. Even though a decrease of total rate of entropy production due reversible and irreversible heat has been observed, Case 7 shows an increase in the Ohmic loss, mainly due to the thicker catalyst layer. Moreover, an increase in the total rate of entropy generation due to latent heat has been increased as less water is transported from the anode to the cathode (i.e. back diffusion) and more water is accumulated at the catalyst layer. Even tough Case 8 has a thinner catalyst layer in comparison to Case 1, an augmentation of the total entropy generation due to Ohmic loss has been observed. This is caused by the higher current density produced and consequently, the ionic transportation is increased.

As the ionic and membrane water content diffusion are directly related and affected by the ionomer volume fraction, the variation of ionomer volume fraction has an impact on the total rate of entropy generation due to Ohmic loss. Even though the catalyst layer in Case 9 is thinner in comparison to Case 1, an increase in Ohmic heat has been observed, mainly due to the increase of the ionic resistance at the catalyst layer. Moreover, despite the increase in ionomer loading has contributed in order to decrease the Ohmic heat, an increase of the total rate of entropy generation due to Ohmic heat has been observed in Case 10, mainly due to the use of a thicker catalyst layer in comparison to the base case.

With respect of the different modes of entropy generation rate, it is clear that both reversible and irreversible heats are the main contributors to the increase in entropy generation. For the cases evaluated in this study, it has been found that thinner catalyst layers act to increase the entropy generation rate due to reversible and irreversible heats. Moreover, thinner catalyst layers are generally

responsible for partially reducing the Ohmic loss, and consequently, an enhancement on the current density is expected.

It is evident from the current results that the catalyst layer properties have significant influences on the entropy generation of an AEM fuel cell. Hence, further investigation of the entropy generation mechanisms present at the catalyst layer will be necessary. Moreover, membrane plays a key role in the entropy generation in AEM fuel cells. Ohmic losses at the membrane are substantial due to its low ionic conductivity and its optimisation will also form the basis of future work.

ACKNOWLEDGEMENTS

The financial support of CAPES (the Science without Borders Project) through the grant no. BEX / 13011-13-8 is gratefully acknowledged.

REFERENCES

1. Gupta, G., K. Scott, and M. Mamlouk, *Soluble Polystyrene-b-poly (ethylene/butylene)-b-polystyrene Based Ionomer for Anion Exchange Membrane Fuel Cells Operating at 70 degrees C.* Fuel Cells, 2018. **18**(2): p. 137-147.
2. Jiao, K., et al., *Three-dimensional multiphase modeling of alkaline anion exchange membrane fuel cell.* International Journal of Hydrogen Energy, 2014. **39**(11): p. 5981-5995.
3. Machado, B.S., N. Chakraborty, and P.K. Das, *Influences of flow direction, temperature and relative humidity on the performance of a representative anion exchange membrane fuel cell: A computational analysis.* International Journal of Hydrogen Energy, 2017. **42**(9): p. 6310–6323.
4. Machado, B.S., et al., *A Three-dimensional Agglomerate Model of an Anion Exchange Membrane Fuel Cell.* Journal of Computing and Information Science in Engineering, 2017.
5. Machado, B.S., M. Mamlouk, and N. Chakraborty, *Three-dimensional agglomerate model of an anion exchange membrane fuel cell using air at the cathode - A parametric study.* Journal of Power Sources, 2019. **412**: p. 105-117.
6. Sciacovelli, A. and V. Verda, *Entropy generation analysis in a monolithic-type solid oxide fuel cell (SOFC).* Energy, 2009. **34**(7): p. 850-865.
7. Rangel-Hernandez, V.H., et al., *Entropy generation analysis of a proton exchange membrane fuel cell (PEMFC) with a fermat spiral as a flow distributor.* Energy, 2011. **36**(8): p. 4864-4870.
8. Naterer, G.F., C.D. Tokarz, and J. Avsec, *Fuel cell entropy production with ohmic heating and diffusive polarization.* International Journal of Heat and Mass Transfer, 2006. **49**(15-16): p. 2673-2683.
9. Kjelstrup, S. and A. Rosjorde, *Local and total entropy production and heat and water fluxes in a one-dimensional polymer electrolyte fuel cell.* Journal of Physical Chemistry B, 2005. **109**(18): p. 9020-9033.
10. Damian-Ascencio, C.E., et al., *Numerical modeling of a proton exchange membrane fuel cell with tree-like flow field channels based on an entropy generation analysis.* Energy, 2017. **133**: p. 306-316.
11. Xing, L., M. Mamlouk, and K. Scott, *A two dimensional agglomerate model for a proton exchange membrane fuel cell.* Energy, 2013. **61**: p. 196-210.
12. Xing, L., et al., *A two-phase flow and non-isothermal agglomerate model for a proton exchange membrane (PEM) fuel cell.* Energy, 2014. **73**: p. 618-634.
13. Wu, H., X.G. Li, and P. Berg, *On the modeling of water transport in polymer electrolyte membrane fuel cells.* Electrochimica Acta, 2009. **54**(27): p. 6913-6927.
14. Deng, H., et al., *Transient analysis of alkaline anion exchange membrane fuel cell anode.* International Journal of Hydrogen Energy, 2013. **38**(15): p. 6509-6525.
15. Lampinen, M.J. and M. Fomino, *Analysis of Free-Energy and Entropy Changes for Half-Cell Reactions.* Journal of the Electrochemical Society, 1993. **140**(12): p. 3537-3546.
16. Weber, A.Z. and J. Newman, *Coupled thermal and water management in polymer electrolyte fuel cells.* Journal of the Electrochemical Society, 2006. **153**(12): p. A2205-A2214.
17. Farran, R. and N. Chakraborty, *A Direct Numerical Simulation-Based Analysis of Entropy Generation in Turbulent Premixed Flames.* Entropy, 2013. **15**(5): p. 1540-1566.
18. Ren, X.M., et al., *Highly Conductive Anion Exchange Membrane for High Power Density Fuel-Cell Performance.* Acs Applied Materials & Interfaces, 2014. **6**(16): p. 13330-13333.
19. Kruusenberg, I., et al., *Non-platinum cathode catalysts for alkaline membrane fuel cells.* International Journal of Hydrogen Energy, 2012. **37**(5): p. 4406-4412.
20. Leng, Y.J., et al., *Alkaline membrane fuel cells with in-situ cross-linked ionomers.* Electrochimica Acta, 2015. **152**: p. 93-100.
21. Park, S., J.W. Lee, and B.N. Popov, *Effect of carbon loading in microporous layer on PEM fuel cell performance.* Journal of Power Sources, 2006. **163**(1): p. 357-363.

22. Afsahi, F., F. Mathieu-Potvin, and S. Kaliaguine, *Impact of Ionomer Content on Proton Exchange Membrane Fuel Cell Performance.* Fuel Cells, 2016. **16**(1): p. 107-125.
23. Prasanna, M., et al., *Effects of platinum loading on performance of proton-exchange membrane fuel cells using surface-modified Nafion (R) membranes.* Journal of Power Sources, 2006. **160**(1): p. 90-96.

- Reversible and irreversible heat are the main sources of entropy production;
- Ohmic heat is highly dependent on the fuel cell hydration;
- Catalyst layer volume plays a major role in the specific rate of entropy generation